DIC-based Full-Field Calibration using LS-OPT®: An Update

[1]Stander,N, [2]Witowski,K, [2]Ilg,C, [1]Basudhar,A, [3]Svedin,Å, [1]Gandikota,I,
[2]Haufe,A, [1]Du Bois,S, [1]Kirpicev,D
[1]Livermore Software Technology Corporation, Livermore, CA
[2]DYNAmore GmbH, Stuttgart, Germany
[3]DYNAmore Nordic, Linköping, Sweden

Abstract

This paper extends a 2017 study on full-field calibration using Digital Image Correlation (DIC) and the Finite Element Method to identify parameters of a material model developed for elastoplasticity. DIC is an optical method which provides full-field displacement or strain measurements for mechanical tests of materials and structures. It can be combined with the corresponding fields obtained from a Finite Element Analysis to identify constitutive properties. The methodology, which involves the solution of an inverse problem, consists mainly of two new core features namely (i) multi-point histories and (ii) suitable curve similarity measures. Multi-point histories are response curves which are evaluated at multiple spatial locations and extracted from simulations and experimental data. To improve on the previously used Euclidean curve distance measure, the Discrete Fréchet (DF), Dynamic Time Warping (DTW) and Partial Curve Mapping (PCM) measures were developed and validated for multi-point histories. An interface to a commercial DIC package, as well as two text-based generic interfaces, was also developed. A tensile test example was used to validate and demonstrate the methodology based on the DIC measurement of spatial point-wise strains. The example validated the code but revealed potential problem areas, such as solution stability, requiring further investigation.

Introduction

The goal of material parameter identification is to characterize the constitutive behavior using experimental results in combination with structural modeling of the test samples. Although rather well established, it is a complex subject which may involve material nonlinearity [1,2], hysteretic behavior (loading and unloading) [2], strain localization [1,3] as well as instability of the calibration [4]. The testing component may also involve full-field optical measurement [1,5,6,7,8,9,10].

A simple and common approach for identifying the parameters of certain types of materials is to use the tensile test, in which a coupon is subjected to a force while being measured for deformation. Both are global quantities. To extract the material properties, the coupon, usually of simple geometry, can be modeled using the Finite Element Method which incorporates the constitutive model to be calibrated.

The methodology for conducting a calibration typically requires the construction of a distance function to quantify the distance between the experimental and computational results, for example the squared Euclidean distance measure:

$$f(\boldsymbol{x}) = \sum_{j=1}^{n} \left[\varphi_j(\boldsymbol{x}) - \tilde{\varphi}_j \right]^2 \tag{1}$$

where $\varphi_j(\boldsymbol{x})$ are the components of a force history or force-displacement vector and n is the number of observation states. The vector $\boldsymbol{x}$ represents the unknown material parameters and the ~ designates the experimental results. The Euclidean distance is minimized using optimization.

Methods and techniques to determine the similarity between time series play a critical role across a vast number of diverse research fields. However, the inferiority of popular measurements like Euclidean and Hausdorff have been illustrated by many authors [11,12,13,14]. For non-functions, such as when loading-unloading occurs, more sophisticated techniques are required such as the *Discrete Fréchet* (DF) method [16], *Dynamic Time Warping* (DTW) [17] or *Partial Curve Mapping* (PCM) [2]. In the current study, the DF, DTW and PCM measures are used as part of a full-field calibration.

The (continuous) Fréchet distance was first defined by Maurice Fréchet in 1906 [16]. In 1994 Eiter and Mannila presented a discrete implementation in order to measure the similarity between two polygonal chains P, Q using only the points along the chains [18]. A popular and intuitive analogy for the discrete Fréchet (DF) distance measurement is a man traversing a path along one curve while walking his dog, which follows the second curve, on a leash. The discrete Fréchet value equals the sufficient length of the leash. DF measures the similarity between curves by taking the minimum of the maximum of all possible edge lengths along a path, which connects all given data points. Mathematically, this can be expressed as

$$DF(P, Q) = min\left\{\max_{i=1,\dots,l}\{d(p_{a_i}, q_{b_i})\}\right\},$$

where $d(\cdot, \cdot)$ denotes the Euclidean distance. The method takes into account the location and ordering of the points, which makes it applicable in cases where the Euclidean method would fail. However, when dealing with curves of different length, the result may be inaccurate since it considers all points in both curves. Furthermore when points are not uniformly distributed, particularly in case of a big gap between two points on a chain, DF will focus on the gap. This non-robust behavior can easily distort the distance value.

Originating in speech recognition in the 1960s a second similarity measure, Dynamic Time Warping (DTW), has been a research topic for scientists of different fields, resulting in many variations of the method [19]. Variations such as FastDTW [20] and the Sakoe-Chiba Band [21] focus on reducing runtime while having an impact on accuracy. In this paper, we focus on the classical DTW approach. DTW calculates the distance between two data sets, which may vary in time, via its corresponding warping path $W = (w_1, \dots, w_l)$. This path is the result of the minimum accumulated distance which is necessary to traverse all points in the curves. The DTW distance value can be formulated as

$$DTW(P, Q) = \min_W\left\{\sum_{i=1}^{l}\delta(w_i)\right\},$$

where $\delta(w_i) = d(p_h, q_k)$ if $w_i = (h, k)$. Note that a higher density of points yields an increased DTW distance, since it is defined as the accumulation of distances. Due to this design, a high distance value might be misleading.

While simple material models can typically be uniquely identified using a tensile and/or shear test, a major difficulty in parameter identification is ill-posedness of the observation equation [4]:

$$A(x) = y\, ; x \in \text{X} \tag{2}$$

in which the mapping A represents the modeling (e.g. a FE model), $x \in \text{X}$ represents the model parameters (the material constants) bounded by the parameter space X and y represents the data (experimental data) in the observable data space Y. This problem is typically solved as a minimization problem [4]:

$$y = \arg\{\underset{y'}{\text{Min}}\, J(y'; x)\} \equiv A(x) \tag{3}$$

In Reference [4] Bui lists important issues to check when solving the inverse problem, namely (i) stability of the solution with respect to variations in the data y as well as with respect to modeling errors and small changes in the model space X (robustness). It should be mentioned that *the inverse problem to determine the parameters x, for given experimental data y, is generally ill-posed*. In material parameter identification, various conditions can cause ill-posedness, for example [4]:

- False experimental data (measurement errors or erroneous data files)
- Incompatible or insufficient data, i.e. there is no set of material parameters that will cause the model to produce results in data space D.
- Noise in the experimental data
- Modeling errors e.g. in the constitutive model or coarse approximation of the model A

These problems are manifested because of the lack of suitable information provided by the chosen test. E.g. providing global information such as a force-displacement curve representing a chosen point or cross-section of a coupon may not be sufficient to characterize a nonlinear material model involving material flow, failure and/or damage. It is also typical of failure behavior to be localized, which eludes capture by global force-displacement data [1]. It is probably safe to assume that the more sophisticated the material model and the phenomena it is intended to model, the more parameters it possesses and the greater the need exists for full-field calibration to capture localized behavior.

While optimization always yields a solution to the unconstrained, but simply bounded, regression problem, the deficiency in the distribution of the input data may result in instability of that solution. It is with this problem, as well as accuracy, in mind that experimental mechanicians, over the last three decades, have introduced full field optical measurement techniques. These allow more comprehensive sampling in order to capture phenomena to which the material parameters have non-zero sensitivity, thereby improving stability of the calibration.

The purpose of these non-contact methods is to measure the spatial distribution of physical quantities such as displacement or strain. Much of the development in this area arose from the improvements made to camera and computer technology as well as analysis techniques such as the Finite Element Method. Multiple optical measurement methods have been forthcoming such as digital holography and speckle interferometry. Magnetic Resonance Imaging (MRI) has been used to characterize myocardial material, see e.g. [9]. The focus of the current paper is an optical measurement method referred to as Digital Image Correlation [10].

Figure 1: Tensile testing equipment and optical measurement system by GOM ARAMIS.
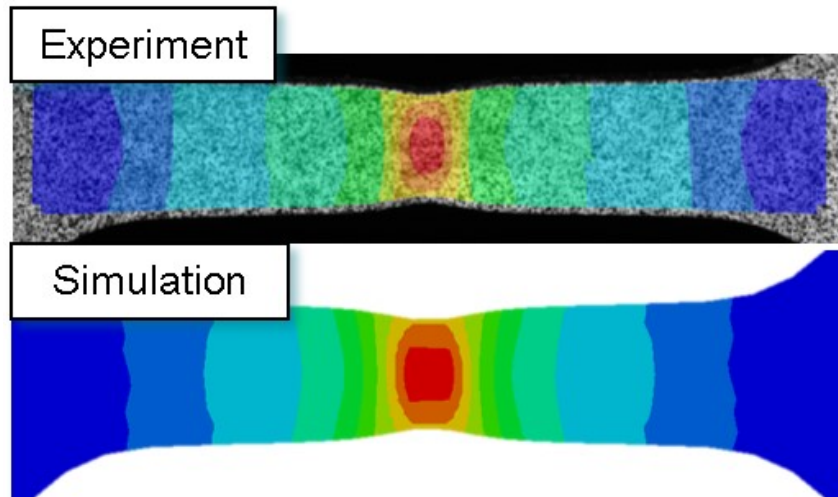
Figure 2: Full field measurement of a tensile test using Digital Image Correlation. Above is the DIC image (GOM ARAMIS) while a strain contour plot is featured below (LS-PrePost®).

Digital Image Correlation (DIC) started to appear in the early 1980s and is an optical measurement method (see Fig. 1 for test setup) which provides full-field displacement measurements for mechanical tests of materials and structures. A specific advantage of this tool is that it exploits numerical images acquired at different stages of loading. As such, it can be used to obtain temporal displacement, deformation or strain fields from an experimental coupon and can be combined with Finite Element Analysis to identify the constitutive properties of a material (see Fig. 2).

Using DIC results, optimization is used to obtain the parameters which will minimize the distance functional involving the measured field and the computed field as components. As expressed for instance in Mahnken et al [1] the functional used is:

$$f(\boldsymbol{x}) = \sum_{j=1}^{n} \left\| \boldsymbol{\varphi}_j(\boldsymbol{x}) - \widetilde{\boldsymbol{\varphi}}_j \right\|^2 \tag{4}$$

where $\boldsymbol{\varphi}_j(\boldsymbol{x})$ is a vector of nodal displacements or strains with dimension equal to the number of spatially distributed observation points and n is the number of observation states. The functional can be augmented to incorporate global force-displacement measurements or any other functional resulting in parameter identification based on a multi-scale DIC (see e.g. [7]).

The current study follows on an earlier paper [22] in which one of the main conclusions indicated a need to improve upon the current use of the Euclidean distance measure. For that purpose, a previously developed algorithm PCM [2] was extended to the full-field application and applied to the same example.

Methodology and software features

While LS-OPT has included parameter identification features since its first commercial release, the current development goal is to significantly enhance these capabilities to enable LS-OPT to accommodate modern testing techniques such as DIC. While full field calibration has been conducted using LS-OPT in the past [9], the current implementation generalizes the feature to enable it to address a greater diversity of problems.

A summary of essential features, most of which have now been implemented in LS-OPT, follows:

1. A core feature of the methodology is the *multi-point history*, a basic mathematical entity representing both spatial and temporal dimensions. Multi-point histories are hyper-curves which are evaluated at multiple locations (possibly thousands) and extracted from simulations and experimental data.
2. To access test data, an interface to the GOM ARAMIS DIC software (using their CSV and XML databases) was developed. Two generic features are provided, namely a fixed format (based on an LS-PrePost history format) *file* based input as well as a more general free format. In the latter, a software tool (GenEx) is provided so that freely formatted fields can be parsed from a text file.
3. A binary tree-based exact nearest neighbor algorithm was developed to efficiently map a test point cloud to an FE model or *vice versa*.
4. Both shell and solid elements are supported. The ability to interpolate fields within an individual finite shell element is incorporated into the mapping approach. Solid element quantities are represented by the values at the element center. Depending on the element size, an error will occur as the optical measuring systems only measure at the surface.
5. Four distance measures are available, namely squared Euclidean and Discrete Fréchet distance, Dynamic Time Warping and Partial Curve Mapping.
6. Error analysis enables the user to assess the size of the mismatch as well as the resulting uncertainty of the parameters.
7. Graphical features are available for previewing test results.
8. Distance contour maps will be provided for post-processing the discrepancy between computed values and experimental quantities (not yet implemented at the time of going to press).
9. Confidence intervals of the material parameters enable the user to quantify their uncertainty (not yet implemented).
10. The DynaStats feature of LS-OPT [11] provides sensitivity analysis and stochastic influence tools to identify spatial strain or displacement sensitivities to individual material parameters. Aside from the obvious use of locating suitable measurement areas, sensitivity analysis also allows the user to compare the significance of different strain measures, e.g. ε_{xx}, ε_{yy} and ε_{xy}.

A more detailed discussion is provided in the following sub-sections.

GOM ARAMIS interface and alignment of DIC points
Since the final test example uses the GOM ARAMIS measurement software, an LS-OPT GOM interface was implemented to define input files, result components and alignment data. The alignment is computed using the least squares formulation shown in the equation:

$$\min_{\boldsymbol{T}} \|\boldsymbol{X}_{\text{Test}}\boldsymbol{T} - \boldsymbol{X}_{\text{FE}}\| \tag{5}$$

to match any number of test points $\boldsymbol{X}_{\text{Test}}$ to corresponding coordinates on the FE mesh $\boldsymbol{X}_{\text{FE}}$. The points in $\boldsymbol{X}_{\text{Test}}$ and $\boldsymbol{X}_{\text{FE}}$ respectively do not have to correspond exactly. The solution of Eq. (5), using Singular Value Decomposition, yields the transformation matrix $\boldsymbol{T}$ which is then used to transform all the test points (see e.g. Fig. 7). The data can also be specified as nodal/point IDs. Three or four points normally suffice, but any number can be specified. Alternatively, the alignment step can be omitted, since LS-PrePost can also be used to pre-align the point set.

Since time is not relevant to the calibration[1], crossplots between kinematic and static quantities are typically used. To enable the creation of cross-plots from the GOM data, both the *X*- and *Y*-components shown in Fig. 3 can be histories or multi-point histories. E.g. a multi-point xx-strain can be crossed with a multi-point yy-strain to create multi-point stress-strain cross-plots or, as in the example that follows in the next section (Fig. 13), the full-field xx-strain can be crossed with the global force history to create multi-point strain-force cross-plots. The same applies to cross-plots of computational fields.
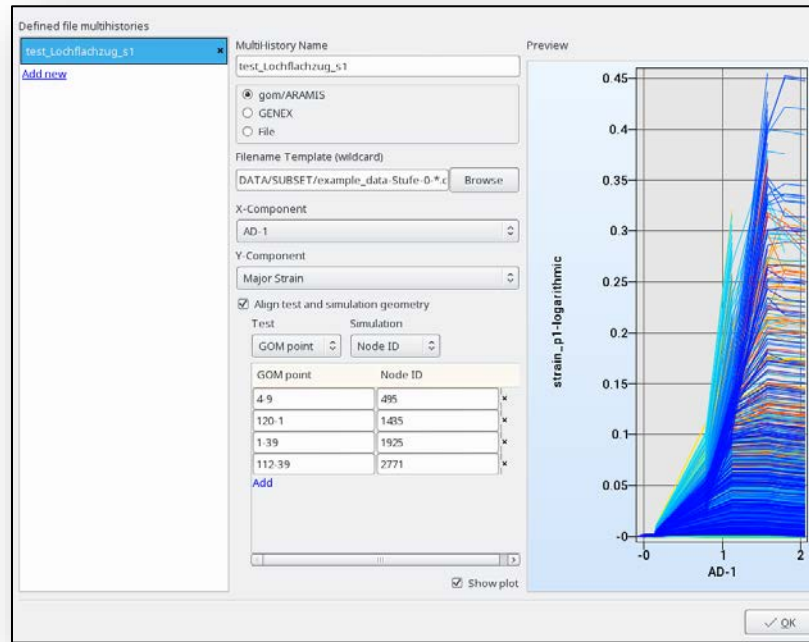
Figure 3: GOM ARAMIS interface in LS-OPT showing alignment input and verification plot of selected test value X- and Y-components.

Multi-point histories
In the GOM ARAMIS option in the multi-point histories interface, each history is computed at a location selected from the test point set in the original, undeformed state. Features are provided to preview the test point alignment (see Fig. 4). E.g. Fig. 5 shows three representative deformation states representing 4557 points extracted from the GOM database for a plate with a hole while Fig. 6 shows the FE mesh with corresponding test points. Fig. 7 shows the outcome of the least squares point alignment using Eq. (5).

---

[1] Simulations are often done as quasi-static, using an implicit method to achieve equilibrium at each state of deformation, a notable exception being rate-dependent materials such as those exhibiting visco-elasticity or -plasticity.
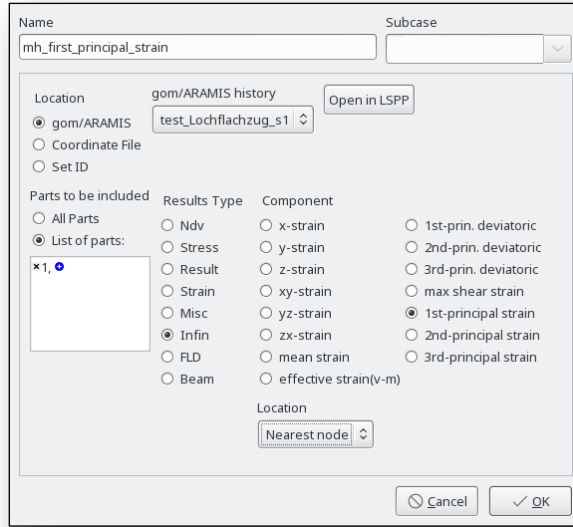
Figure 4: Multi-point history interface enabling the definition of the response type and location data. Location type can be defined as 'nearest node' or 'element'. In the latter option, the result is interpolated at the precise location within the nearest element.
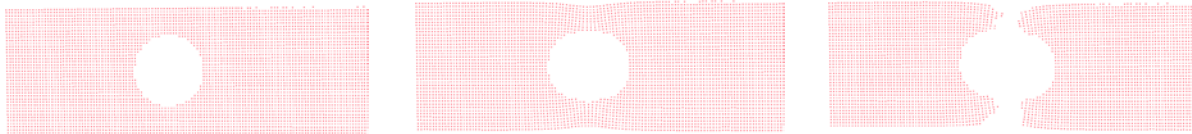

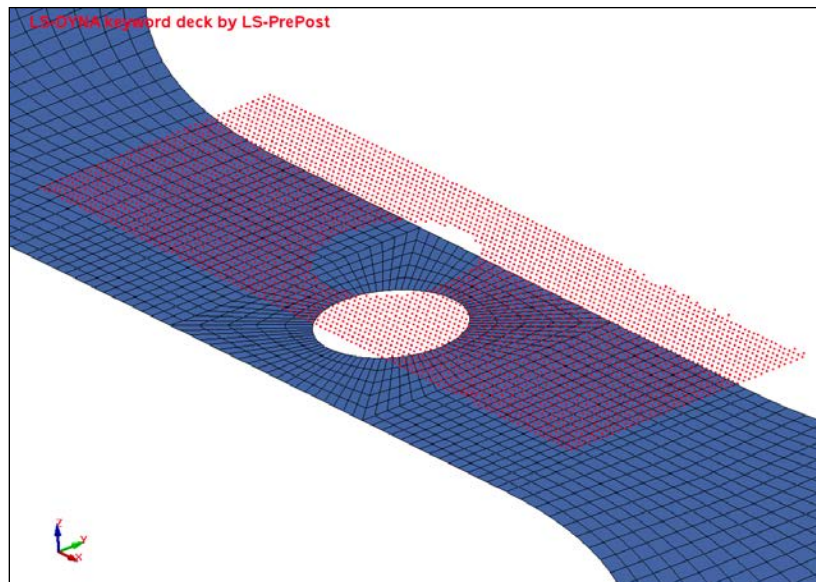Figure 5: Selected deformation states from GOM/ARAMIS output.

Figure 6: Example of test point mapping showing test point set (red) of 4557 points in relation to the Finite Element mesh.
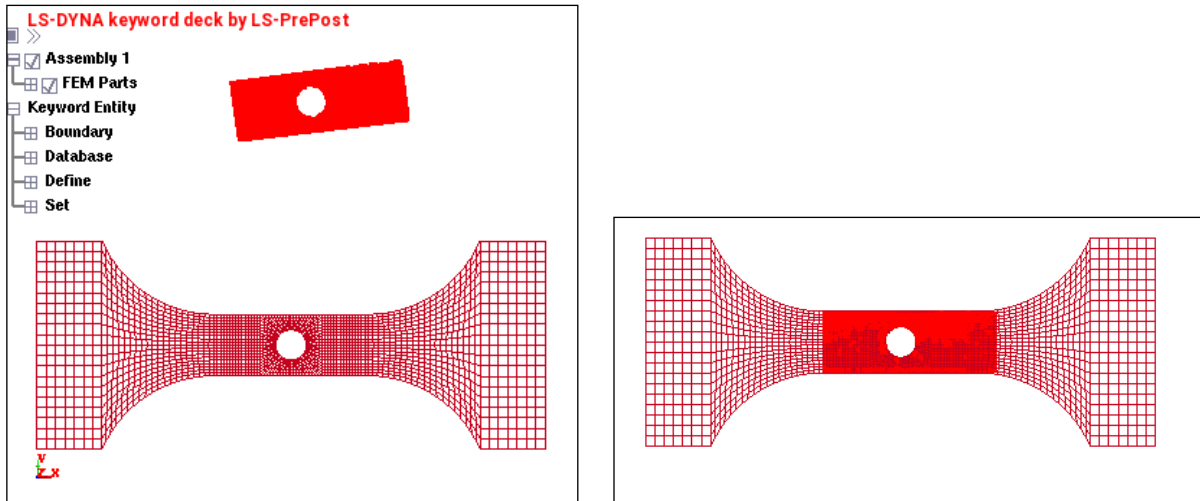
Figure 7: Interactive feature for verification of least squares test point alignment. The starting test point location (in bright red) is shown on the left.

Mapping test points to a FE mesh

A given aspect of DIC is that the experimental points and FE nodes do not spatially coincide (see e.g. Figs. 6 and 15). Hence, after the point set has been aligned with the FE mesh, they then have to be individually mapped to the nodes. The LS-OPT algorithm enables mapping in 3 dimensions using a binary tree. The approach allows for an exact nearest neighbor search with the ability to map 10^7 query points to 10^7 reference points in reasonable time (suitable for interactive use). Practical examples encountered thus far were handled virtually instantaneously.

As a further enhancement to the nearest neighbor mapping, a distance tolerance can be set so that only data sets associated with nodes close to experimental points are used to compute the similarity measure. An additional measure to circumvent this problem, the ability to interpolate fields *within* each individual finite shell element has also been incorporated into the mapping approach. This is especially important for coarse meshes or high resolution DIC. Obviously, there could still be some discretization error, so the finer the FE mesh, the more accurate the interpolated value. The ideal mesh would be one which exactly coincides with the DIC points.

Example: Tensile test

An example of a tensile test was selected to test and demonstrate the full-field calibration feature in LS-OPT (Figs. 1 and 8). The example is the same as used in Reference [22] although multiple distance measures have now been validated and a switch has been made to the Genetic Algorithm in an attempt to improve convergence and accuracy.

Fig. 9 shows the force-displacement trajectory as well as the strain contours at the time state depicted in the plot. The necking phenomenon is clearly visible from the test images in Fig. 9.
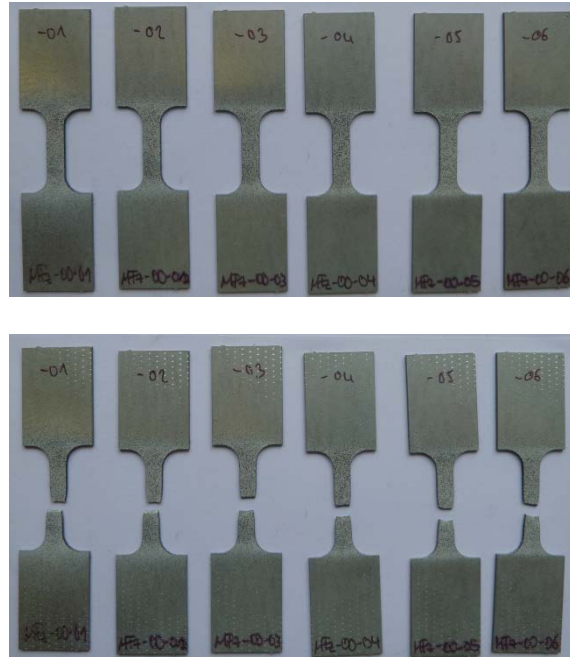
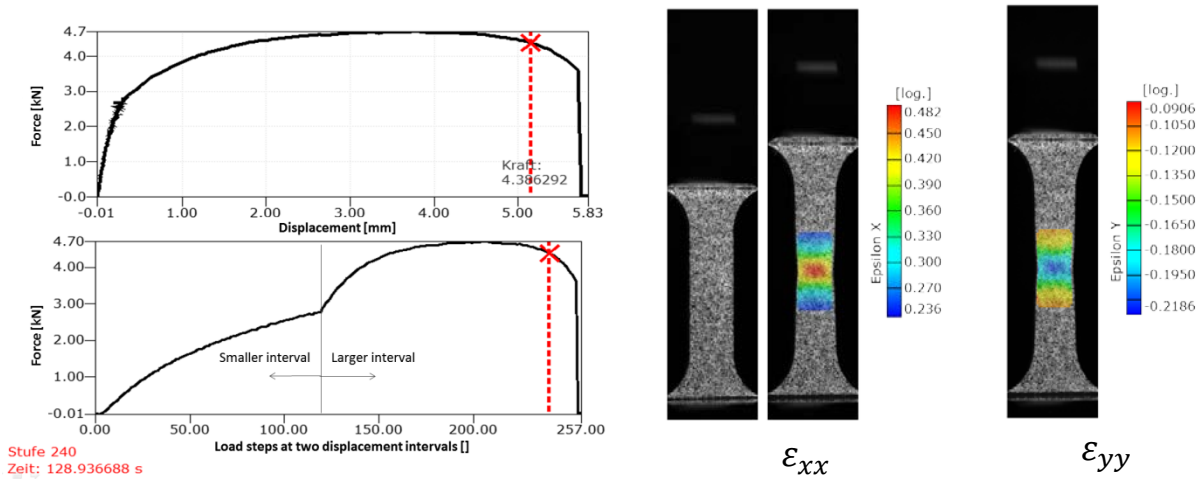Figure 8: Test coupons for a tensile test (0° w.r.t. rolling direction) (Sample numbers MFz-00-*)

Figure 9: Sample MFz-00-01: Force-displacement diagram and DIC contour plots for xx- and yy-strains.

Simulation

A Finite Element model was created in LS-DYNA® [23] to model a typical coupon (Fig. 8) subjected to a tensile force. The material model uses the von Mises yield locus and a Hockett-Sherby flow curve formula for extrapolation beyond the point of a uniform strain state:

$$f(\varepsilon_p) = A - Be^{-C\varepsilon_{pl}^N} \tag{6}$$

where A, B C and N are material constants. C_1-continuity is assumed at the flow transition following the uniform strain state which removes the requirement to incorporate A and B in the optimization that follows.

Validation

This section describes a validation of the implementation, but also compares the results obtained using a single global force-displacement curve vs. full-field strain data.

Global force vs. displacement:
A problem based on synthetic test data was first constructed by creating a target curve from a simulation using material properties fixed at $[C, N] = [0.5, 0.5]$. A subsequent optimization was done from a different starting point in an attempt to recover the target curve. The FE model based on a test coupon and corresponding global load-displacement target curve are shown in Fig. 10.
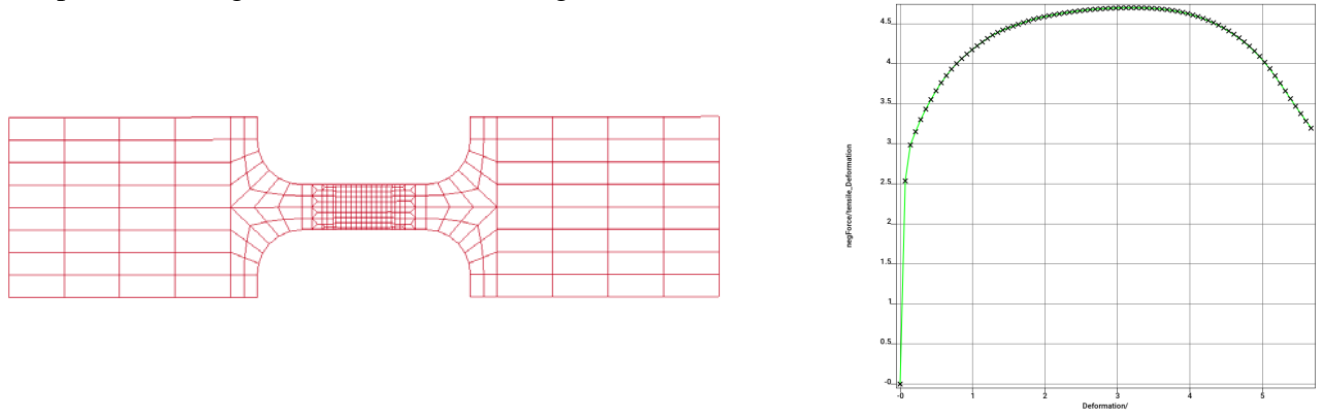

Figure 10: Finite Element mesh with corresponding global force-displacement curve based on $[C, N] = [0.5, 0.5]$. The target curve is represented by the ✕'s.

Since the problem has only two variables, the PCM distance function can be displayed in three dimensions (Fig. 11). The two pictures on the right show the relatively flat valley suggesting near instability of the problem.

A Genetic algorithm was used to conduct a direct optimization using a population size of 30 and iteration limit of 100. The GA procedure is set to stop if the solution does not improve over 50 iterations. Table 1 shows that the target values $[C, N] = [0.5, 0.5]$ are fully recovered by the GA.
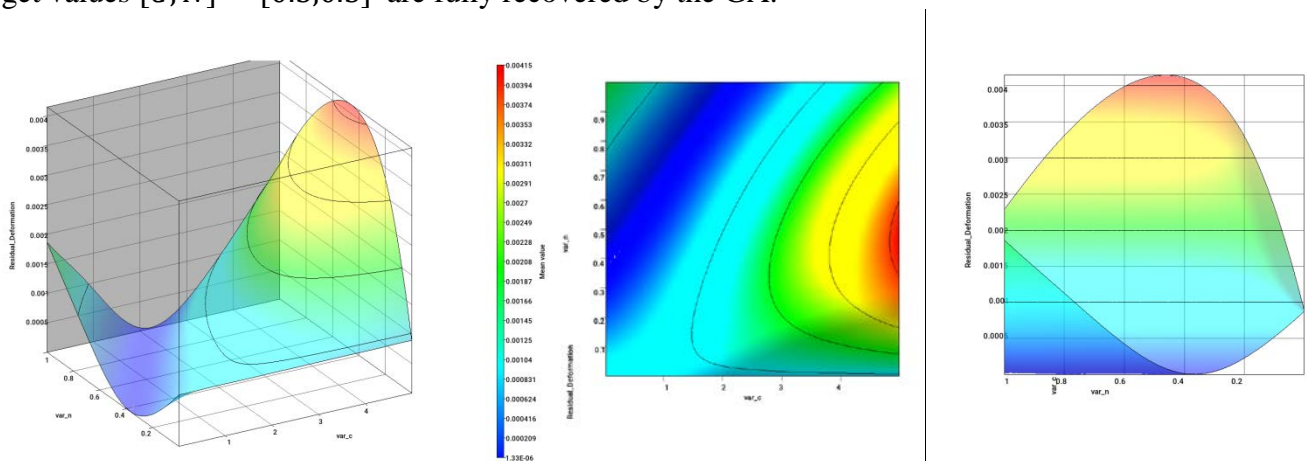

Figure 11: Example based on synthetic test data: Neural Network used to demonstrate the instability of the optimal solution when minimizing the PCM distance measure to match the global x-displacement. RMS Error of the Neural Network fit = 0.0018 (0.454%) with $R^2 = 1.0$.

Table 1: Validation using a target force-displacement curve based on $C = 0.5$ and $N = 0.5$. Optimization conducted with the Genetic Algorithm using a population size of 30 with a 100 generation limit.

	C^*	N^*	ε
PCM	0.500	0.500	3×10^{-10}
Exact	*0.500*	*0.500*	*0*

As a further demonstration of the relative instability, two individual points, with values significantly different from the exact solution, were chosen in the valley. The simulation results are tabulated below (Table 2). Sampling point **#1** as well as its corresponding force-displacement curve is shown in Fig. 12. The computed result is very close to the test result, although a small discrepancy is noticeable at the tail end of the curve.

Table 2: Sample tests, both chosen with relatively small residuals using a target force-displacement curve based on $C = 0.5$ and $N = 0.5$.

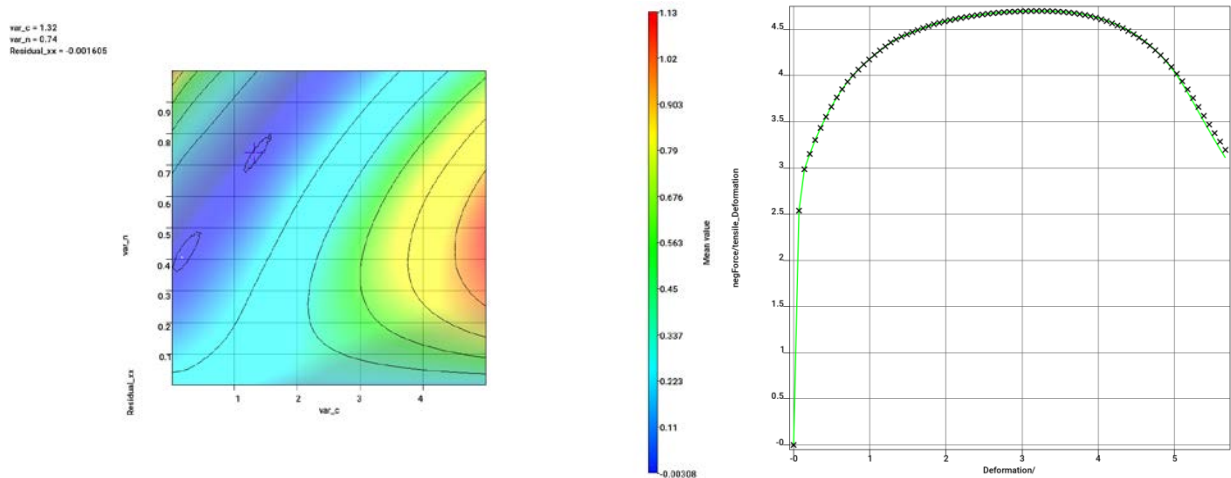| Samples	C	N	ε
#1	1.32	0.74	5×10^{-6}
#2	1	0.6	3×10^{-5}
Exact	*0.500*	*0.500*	*0*

Figure 12: Example based on synthetic test data: curve similarity for Point #1: $[C, N] = [1.32, 0.74]$ chosen to be in the residual valley remote from the optimal point (shown as a $+$ in the picture on the left). Note the slight discrepancy, mainly at the tail end of the green curve on the right (also compare with Fig. 10). The target curve ($\times$) is based on $[C, N] = [0.5, 0.5]$.

Full-field force vs. strain:
The question arises whether a full-field calibration would improve the stability of the problem. Hence, in the second phase, a full body strain field consisting of both ε_{xx} and ε_{yy} based on $[C, N] = [0.5, 0.5]$ is used as a target multi-point curve set. In this phase, three similarity measures were validated using the full-field calibration method, namely the Discrete Fréchet, DTW and PCM measures.

Fig. 13 suggests that the example might be less unstable, but a relatively flat valley roughly connecting $[C, N] = [0.01, 0.4]$ with $[1.8, 1.0]$ (center in Fig. 13) is still present. The rightmost picture in Fig. 13 illustrates the degree of instability in the blue zone. The dark red cube represents the predicted optimum.
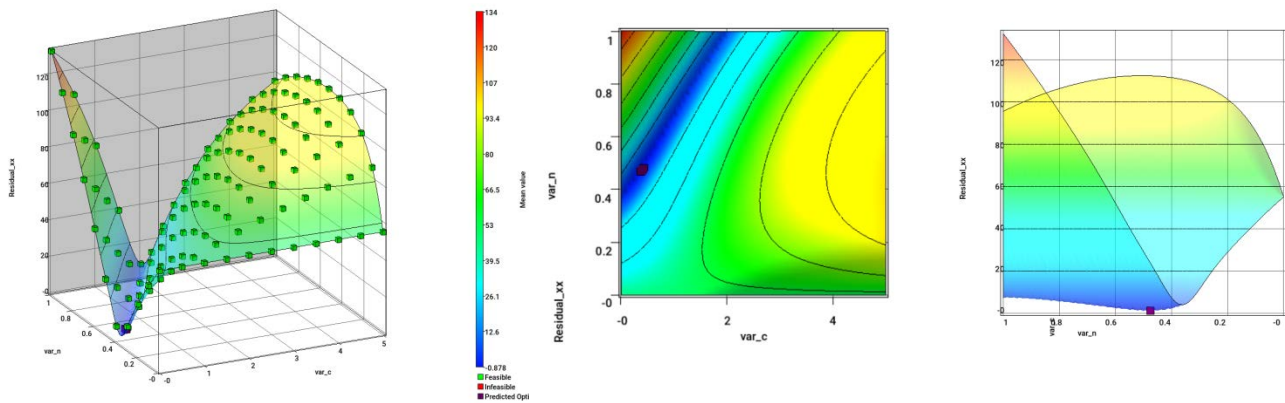

Figure 13: Example based on synthetic test data: Neural Network used to demonstrate the instability of the optimal solution for matching ε_{xx} when minimizing the Discrete Fréchet distance measure (instability is also present using the other distance measures discussed in this study). The picture on the far left also shows the 121 simulation points used to compute the Neural Network. (RMS error = 0.00053, $R^2 = 1.0$.)

Fig. 14 compares the three distance measures for both matching ε_{xx} and ε_{yy} as a function of global force. As expected, the distance functions of both ε_{xx} (the force direction) and ε_{yy} are very similar, and these functions are also similar for the three distance measures (thereby validating the measures themselves). A minor exception is that the PCM valley is noticeably less narrow than that displayed by DF and DTW.

Table 3 provides a comparison of the optima obtained using a GA. The target values for C and N are almost perfectly recovered, thereby validating the implementation.
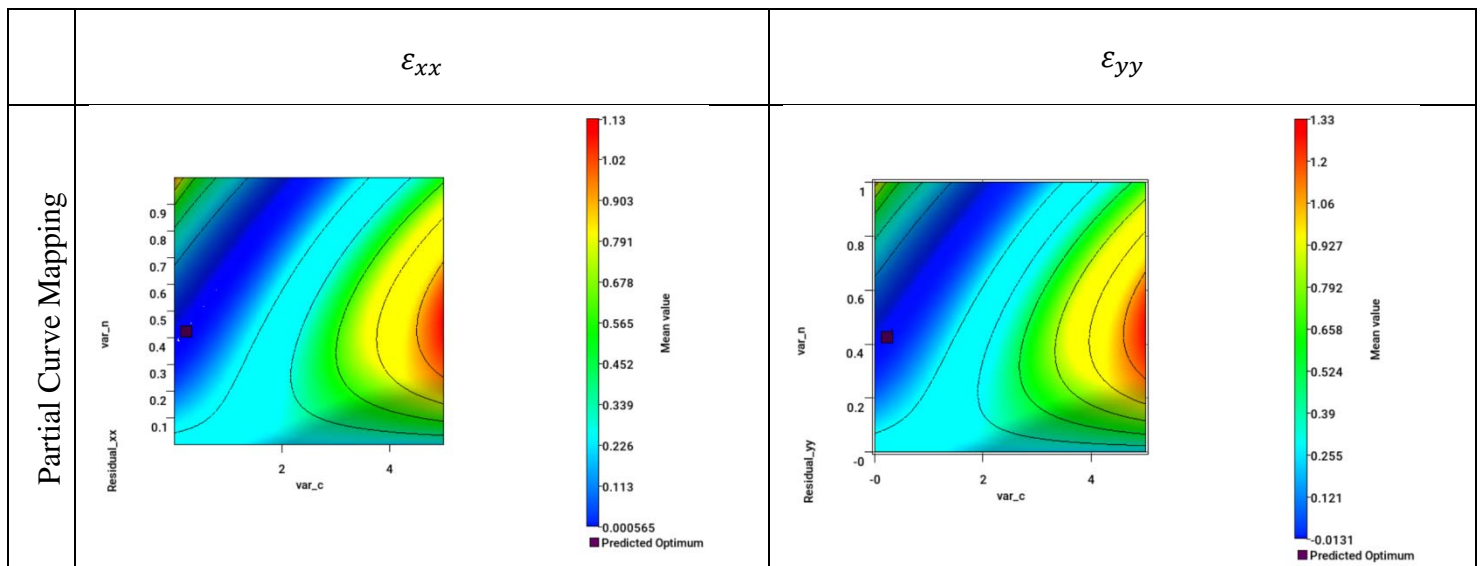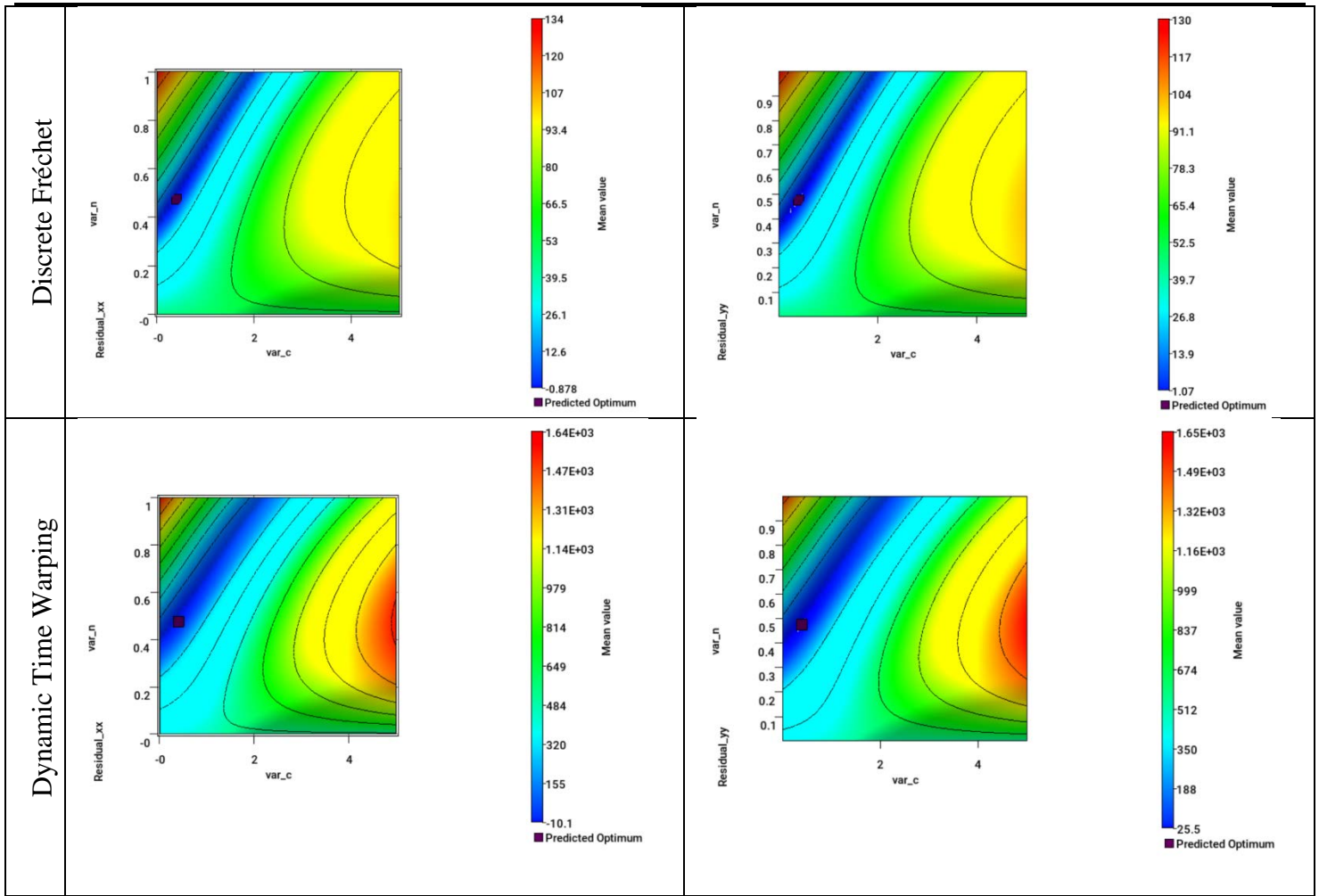
Figure 14: Comparison of Neural Network approximation models representing the distance functions of ε_{xx} and ε_{yy}. The dark red point near the [0.5,0.5] coordinate depicts the optimum.

Table 3: Validation results using a problem based on synthetic test data: A comparison of similarity measures with the optimal values computed using a full-field target curve set initially computed at $C = 0.5$ and $N = 0.5$. Optimization conducted with the Genetic Algorithm using a population size of 30 and a 100 generation limit.

	C^*	N^*
PCM	0.502	0.501
DF	0.500	0.500
DTW	0.497	0.499
Exact	*0.500*	*0.500*

Calibration using experimental data

Finally the material model was calibrated using the DIC results of a laboratory experiment. The LS-OPT setup required alignment of the 391 measured points with the FE mesh as shown in Fig. 15. The force vs. point-wise ε_{xx} strain curves are shown in the previewing feature depicted in Fig. 16. Each curve represents a measuring point as shown in black in Fig. 15. For the optimization, a cross-plot was defined using multi-point histories to represent the global force vs. point-wise strains. The incorporation of the force ensures that both statics and kinematics are incorporated into the behavior.

The optimization problem was set up with parameters C and N as variables and with the objective to minimize the distance function f [Equation (4)]. This defines the ideal of matching ε_{xx} at each point and each deformation state. For maximum accuracy, and because the function evaluations are inexpensive, the optimization was conducted using the Genetic Algorithm in LS-OPT [11] using default settings.

Real experiments present additional challenges to parameter identification implying that the choice of similarity measure is important. Because of the possibility of a partial curve overlap, the PCM method was chosen for the calibration. The accuracy of PCM can be significantly affected by noise (which affects the curve length) but, in this example, experimental noise does not seem to play a major role (see e.g. Figure 16). The reason the Discrete Fréchet and DTW methods were disregarded for this example is because they can be significantly affected by a length difference of the matching curves. The Euclidean distance method was also disregarded because the vertical drop-off of a large number of curves in the post-yield phase defies the use of an ordinate-based distance measurement (see also Fig. 16).
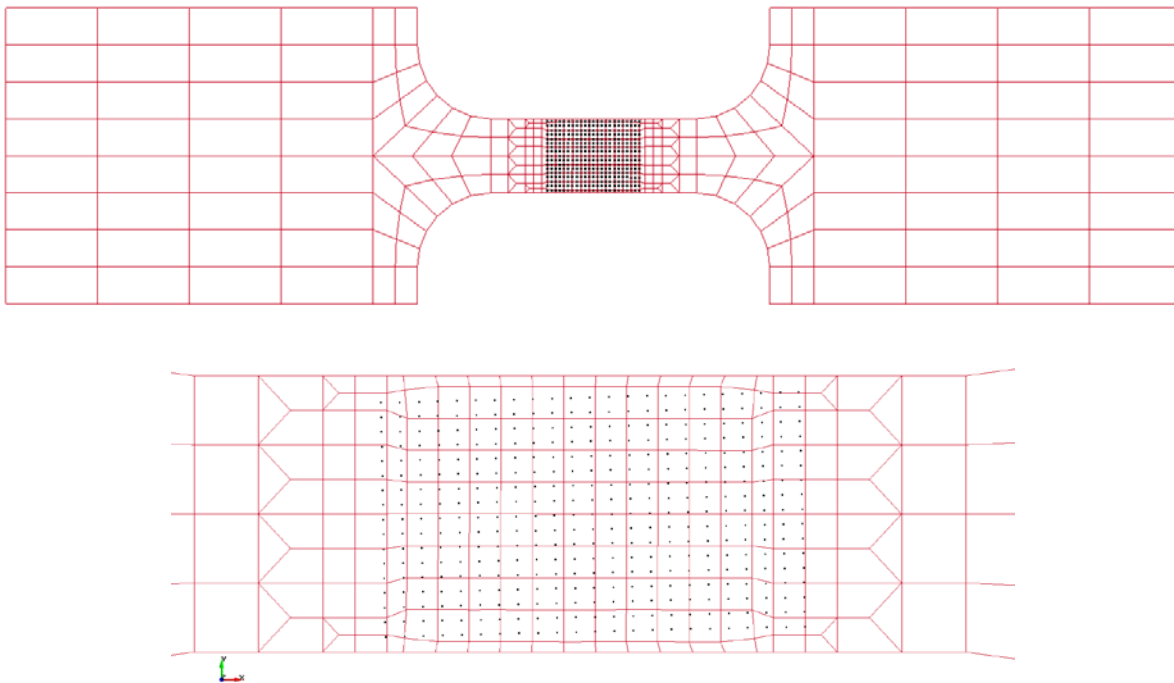

Figure 15: Finite element model of the coupon specimen (red) shown with 391 superimposed optically measured points at the center (black).
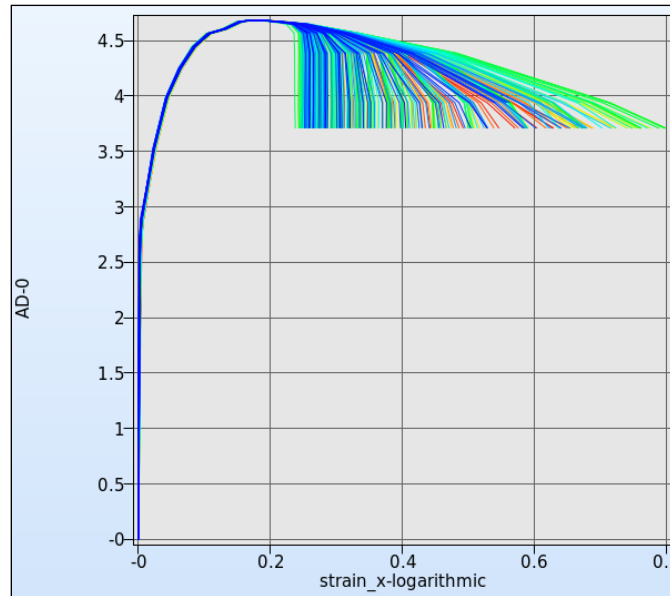
Figure 16: Preview of the multi-point curve: the force (AD-0) vs. full-field logarithmic xx-strain as rendered in a previewing feature of the GOM/ARAMIS interface in LS-OPT. Each curve represents a single measuring point.

Results and observations

The optimization history of the distance function is shown in Fig. 18 while Table 4 shows the optimal results computed using the GA and FFNN. The starting point was the initially estimated values of $C = 0.5$ and $N = 0.5$ The non-zero value of the distance measure (0.02356), also seen in Fig. 17, indicates a failure to exactly fit the material model to the experimental data. Possible reasons for the lack of fit are discussed in detail in the summary and conclusion. Potential instability is noticeable in Fig. 17.
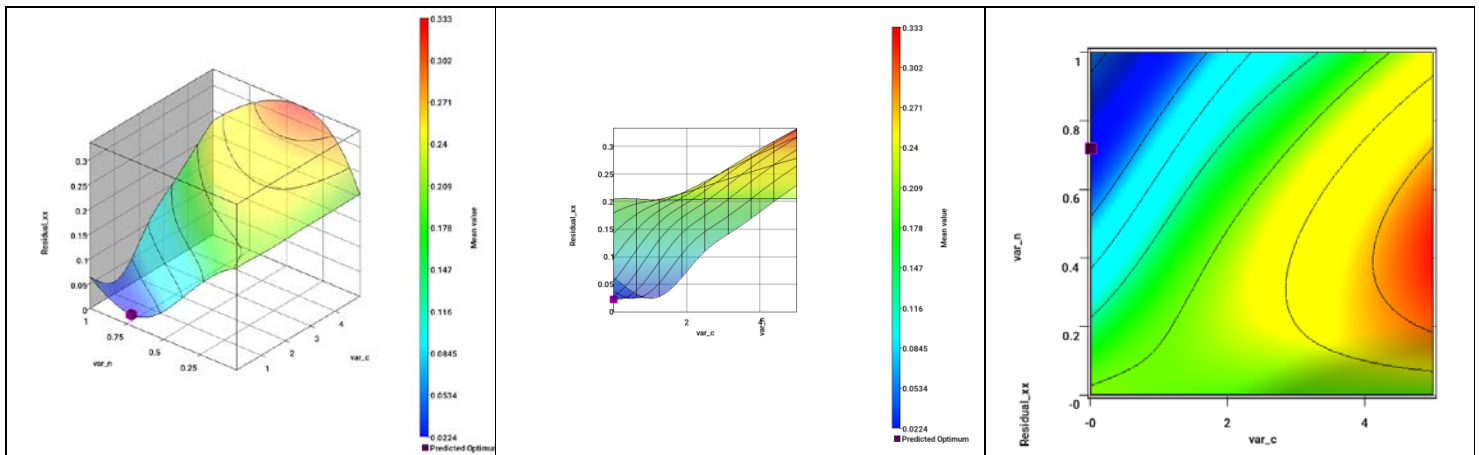

Figure 17: Neural Network approximation of the PCM distance function shown with optimum. Note non-zero residual at the optimum.
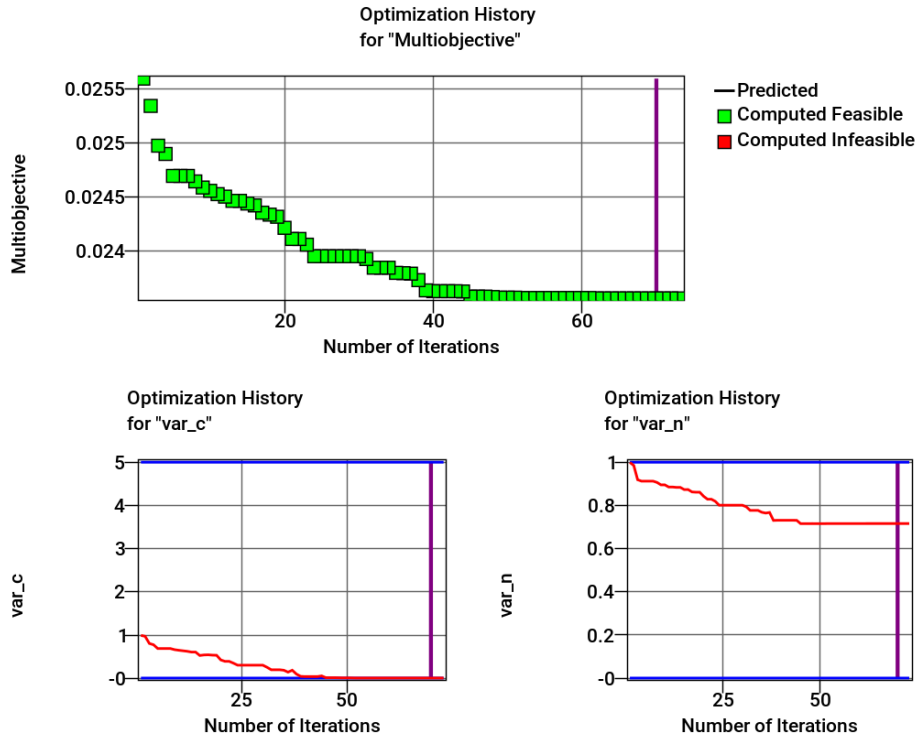
Figure 18: Optimization history of the distance function, Note: the first point is already the best point of the first generation random sample of 30. (from LS-OPT)

Table 4: Optimal parameters when using experimental data as input. Optimization conducted using Genetic Algorithm (30×73 simulations) as well as a Feedforward Neural Network (FFNN) (11×11 sampling grid = 121 simulations). ε Represents the minimum value of the measure. PCM was used as a distance measure.

	C^*	N^*	ε^*
GA	0.0106	0.716	0.02356
FFNN	0.0100	0.718	0.02357

Summary and Conclusions

A parameter identification run was executed using the LS-OPT optimization tool incorporating distance functions based on spatially distributed multi-point histories and DIC experimental results obtained from a tensile test. The calibration is based on a simple example with two variables.

The test example provided here was intended as a working example during the development and is considered sufficient to validate the parameter identification code. However, it is not highly illustrative of the benefit of using DIC, since the experimental points fall in a region of fairly uniform deformation. Therefore, for calibration, it is expected that there would not be much difference in using a global force-displacement curve in comparison with using a full ε_{xx} strain field. It also appears that the addition of ε_{yy} does not have any significant effect on the stability of the problem. It is not immediately clear why the problem is unstable, but it likely has something to do with the chosen constitutive law. To address this and other questions, future work will attempt to incorporate more complex material models as well as more suitable experiments.

A more detailed analysis of the issues, with a view to address them in future development, follows:

1. **Stability and Uniqueness**. The example, which demonstrates a near instability of the solution, highlights the possibility of ill-posedness of the inverse problem for material calibration. Non-uniqueness of the solution is a result of instability, but non-uniqueness can also occur in stable problems. To find a unique solution, it is recommended to use a global optimization algorithm such as the GA.
2. **Curve matching technique** (distance measure). It is apparent that response curves can have very steep, near vertical, post-yield behavior which presents a difficulty for Euclidean measures. As a consequence, some of the curve data may be inadvertently neglected. For this reason, Partial Curve Mapping was used. Other distance measures such as Dynamic Time Warping may also be suitable, but could be problematic if there is a significant length difference between the curves.
3. **Noise**. Noise may emanate from discretization error and/or experimental error. Another source could be the proximity of test points with respect to the extraction locations on the FE model. For this reason, element interpolation was incorporated to extract values from the exact location in the model. Noise will cause a non-zero residual error of the distance function, but also defeats the utility of curve length based distance measures such as Partial Curve Mapping.
4. **Modeling error**. It is possible that, in addition to noise, the material model does not represent the experimental response with sufficient accuracy. This is a bias or modeling error associated with a non-zero minimal curve distance value.
5. **Finite Element discretization error**. The FE mesh provided for the example is somewhat coarse, possibly resulting in a discretization error. This may be especially true because triangular elements are used in the transitions. An obvious remedy would be to increase the fineness of the mesh and to use only higher order triangles or quadrilateral elements.

Future work is also likely to include the following:

1. **Confidence intervals of the parameters**. It is suggested that confidence intervals be calculated for the parameters, a function which requires the calculation of the gradients (with respect to the parameters) of the multi-point histories at the optimal solution x^*. The confidence intervals quantify the degree to which the optimal value of a parameter can be trusted. The computation of confidence intervals requires response surfaces to be constructed at every location and deformation state. This is potentially expensive in terms of computational time.
2. **Sensitivity**. For test coupons designed for localized deformation, a methodology that can be used to investigate sources of instability is sensitivity analysis. In LS-OPT DynaStats [11] the spatial sensitivity (or stochastic influence) contours can be studied to determine spatial locations where sensitivities of response types such as ε_{xx} and ε_{yy} to the individual material parameters are highest. DynaStats is a general tool for previewing the suitability of response field types by allowing the user to study the evolution, over time, of their spatial distribution and relative importance.
3. **Variability.** Since experiments rarely involve a single coupon, future work will also focus on incorporating replicated experiments to assess their influence on the variability of the optimal parameters.

Acknowledgement

References

[1] Mahnken, R., Stein, E. Parameter Identification for Finite Deformation Elasto-Plasticity in Principal Directions, *Comput. Methods Appl. Mech. Engrg*, 147, 17-39, 1997.

[2] Witowski, K., Stander, N. Parameter Identification of Hysteretic Models Using Partial Curve Mapping, *Proceedings of the 12ᵗʰ AIAA Aviation Technology Integration and Operations Conference and 14ᵗʰ AIAA/ISSMO Multidisciplinary Analysis and Optimization Conference*, Indianapolis, Indiana, 2012.

[3] Desrues, J., Réthoré, J. *Full Field Measurements and Identification in Solid Mechanics*, *Chapter 14: Characterization of Localized Phenomena*, 379-409, Eds. Grédiac, M., Hild, F., Wiley, 2013.

[4] Bui, H.D. *Inverse Problems in the Mechanics of Materials, An Introduction*, CRC Press, Boca Raton, London, 1994).

[5] Pagnacco, E., Moreau, A., Lemosse, D. Inverse Strategies for the identification of elastic and viscoelastic material properties using full-field measurements, *Materials Science and Engineering*, Vol. 452-453, 737-745, 2007

[6] Leclerc, H., Périé, J.-N., Roux, S., Hild, F. Integrated Digital Image Correlation for the Identification of Mechanical Properties, *MIRAGE 2009, LNCS 5496*, 161-171, 2009, A Gagalowicz and W. Philips (Eds.), Springer-Verlag, 2009.

[7] Passieux, J.C., Bugarin, F., David, C., Périé, J.-N., Robert, L. Multiscale Displacement Field Measurement Using Digital Image Correlation: Application to the Identification of Elastic properties, https://hal.archives-ouvertes.fr/hal-00949038, 2014.

[8] Gu, J., Cooreman, S., Smits, A., Bossuyt, S., Sol, H., Lecompte, D. and Vantomme, J. Full-field optical measurement for material parameter identification with inverse methods, *High Performance Structures and Materials III, WIT Transactions on the Built Environment*, 85, 2006. doi10.2495/HPSM06024.

[9] Stander, N. *The identification of myocardial material parameters from spatial tagged MRI strain data using LS-OPT and LS-DYNA*, Report, LSTC In cooperation with J. Guccione, Cardiac Mechanics Lab, UCSF, 2006.

[10] Bornert, M., Hild, F., Orteu, J.-J., Roux, S. *Full Field Measurements and Identification in Solid Mechanics*, *Chapter 6: Digital Image Correlation*, 157-190, Eds. Grédiac, M., Hild, F., Wiley, 2013.

[11] Stander, N., Roux, W.J., Basudhar, A., Eggleston, T, Craig, K.-J. *LS-OPT Users Manual, Version 5.2*. December 2015.

[12] Aach, J. & Church, G. (2001). Aligning gene expression time series with time warping algorithms. Bioinformatics. 17,495-508.

[13] Bar-Joseph, Z., Gerber, G., Gifford, D., Jaakkola, T. & Simon, I. (2002). A new approach to analyzing gene expression time series data. In Proceedings of the 6th Annual International Conference on Research in Computational Molecular Biology, 39-48.

[14] Yi, B.K., Jagadish, H. & Faloutsos, C. (1998). Efficient retrieval of similar time sequences under time warping. In *ICDE '98*, 23-27.

[15] Zhang Zhang, Kaiqi Huang and Tieniu Tan, Comparison of Similarity Measures for Trajectory Clustering in Outdoor Surveillance Scenes, 18th International Conference on Pattern Recognition (ICPR'06), Hong Kong, 2006, 1135-1138.

[16] Fréchet, M..Sur quelques points du calcul fonctionelles, *Rendiconti del Circolo Mathematico di Palermo,* 22, 1-74, 1906.

[17] Berndt, D.J., Clifford, J. Using Dynamic Time Warping to Find Patterns in Time Series. *From: AAAI Technical Report WS-94-03*

[18] Eiter, Thomas, Heikki Mannila. Computing discrete Fréchet distance. Tech. Report CD-TR 94/64, Information Systems Department, Technical University of Vienna, 1994.

[19] Meinard Müller. *Information Retrieval for Music and Motion*. 69-84. Springer, 2007.

[20] Stan Salvador and Philip Chan. FastDTW: Toward Accurate Dynamic Time Warping in Linear Time and Space. Intell. Data Anal., 11(5):561-580, Oct. 2007

[21] H. Sakoe and S. Chiba, Dynamic programming algorithm optimization for spoken word recognition, in IEEE Transactions on Acoustics, Speech, and Signal Processing, 26 (1), 43-49, Feb. 1978.

[22] Stander, N., Witowski, K., Ilg, C., Haufe, A., Helbig, M., Koch, D. Application of Digital Image Correlation To Material Parameter Identification, *Proceedings of the 12ᵗʰ World Congress on Structural and Multidisciplinary Optimization,* Braunschweig, Germany, June 5-9, 2017.

[23] Hallquist, J.O. *LS-DYNA Users Manual, Livermore Software Technology Corporation*.